

# Validation of DNS and RANS Approaches on Turbulent Natural Convection against the BALI-Metal Experiment

Boshen Bian<sup>1</sup>, Walter Villanueva<sup>1,2</sup>

<sup>1</sup>Division of Nuclear Power Safety, Royal Institute of Technology (KTH), Sweden

<sup>2</sup>Nuclear Futures Institute, Bangor University, United Kingdom

## Abstract

During severe accident scenarios in nuclear reactors, the core and internal structures can melt down and relocate to the lower head of the reactor pressure vessel (RPV), where they interact with any remaining coolant. This process can lead to the formation of a stratified molten pool, which is also called corium. It consists of dangerously superheated oxidic and metallic liquids, which imposes thermo-mechanical loads on the vessel wall. Typically, the molten pool separates into distinct layers, with a lighter layer of metallic materials on top and a denser layer of oxides at the bottom. The metal layer acts as a heat sink, absorbing heat from the heat-generating oxide layer and conducting it towards the inner wall of the RPV. This concentrated heat load to the vessel is known as the focusing effect.

This study conducts numerical simulations of the turbulent natural convection flow in a fluid layer undergoing both top and lateral cooling based on the BALI-Metal 8U experiment. Different methods were employed, including Direct Numerical Simulation (DNS) and three Reynolds-Averaged Navier-Stokes (RANS) models:  $k-\omega$  SST, standard  $k-\epsilon$ , and Reynolds stress equation model (RSM). The simulation results are compared with experimental data, and the RANS models are assessed using the DNS results. The results reveal that DNS is able to reproduce a two-distinct region flow structure similar to the experimental observations. The  $k-\omega$  SST model shows similar flow patterns and turbulent kinetic energy (TKE) profile as the DNS results. Regarding the temperature field, all simulations overpredict temperature compared to the experimental data, with DNS providing the closest results. The turbulent heat flux (THF) result shows the RANS models are incapable of accurately modelling THF in turbulent natural convection flow. The heat flux analysis demonstrates that DNS achieved good agreement with experimental data in terms of heat flux distribution and energy balance, while the RANS models underestimate the focusing effect. Furthermore, DNS captures the transient maximum heat flux on the lateral cooling wall, which is higher than the time-averaged value, an important factor for estimating the focusing effect.

**Keywords:** Corium, Focusing effect, Natural convection, Direct Numerical Simulation (DNS), Reynolds-Averaged Navier-Stokes (RANS)

## 1. Introduction

In a hypothetical severe accident at a nuclear power plant, the reactor core and some internal structures could melt and move to the bottom part of the reactor pressure vessel (RPV). Due to the heat released by the fuel material, the debris can melt again and form a molten pool called corium. To manage such accidents, a strategy called In-vessel Retention (IVR) is used[1]. It involves cooling the corium from the outside using water, and this method is employed in both low- and medium-power reactors as well as in the design and construction of higher power reactors. A key requirement for successful IVR is to ensure that the heat produced by the corium does not exceed the Critical Heat Flux (CHF) allowed for the external cooling with water. Therefore, it is crucial to study how the corium behaves in terms of heat and fluid flow in order to predict how the heat is distributed on the vessel.

Typically, the corium tends to separate into distinct layers, where a lighter layer of metallic materials forms on top of a denser layer composed of oxides, as depicted in Figure 1. The oxidic layer generates heat internally due to the release of decay heat and heat resulting from chemical reactions. Conversely, the metallic layer normally lacks an internal heat source, allowing it to act as a heat sink. It absorbs heat from the overlying oxide layer and conducts it towards the inner wall of the reactor pressure vessel [2]. Figure 2 illustrates the heat transfer processes that occur within the corium and between the corium and the vessel wall. Since the metallic layer has high thermal diffusion, the heat flux ( $q_{M \rightarrow W}$ ) from this layer to the PRV inner wall can be relatively substantial, leading to a concentrated heat load. This concentrated heat load is also called focusing effect, which poses a significant threat to the IVR strategy. Hence, it is vital to analyze the thermal and fluid behavior of the metallic layer within the corium.

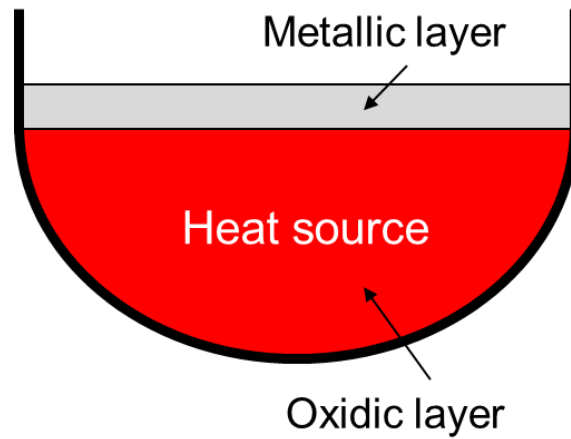


Figure 1 Schematic of the two-layer molten pool

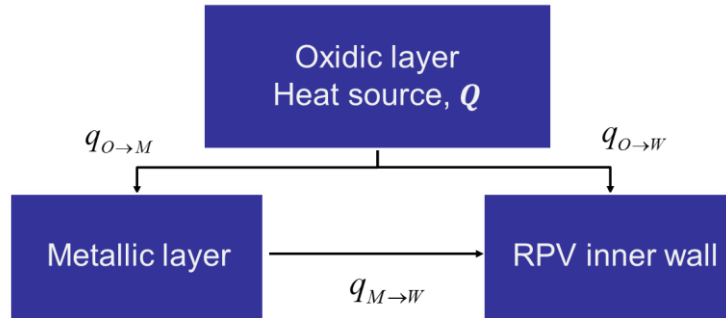


Figure 2 Heat balance in two-layer corium

Within the molten pool, the behavior of the corium in terms of heat and fluid flow is classified as natural convection. This phenomenon is primarily driven by the buoyancy force generated from temperature differences. When these temperature differences are caused by the boundary conditions, it is known as Rayleigh-Bénard (RB) convection. In the case of corium, the metallic layer in the two-layer corium pool experiences heating from the bottom oxidic layer and cooling at the other boundaries, resulting in the occurrence of RB convection in the metallic layer. A well-known experiment called the BALI-Metal experiment was conducted to investigate the natural convection behavior in a fluid layer contained in a rectangular cavity[2, 3]. In this experiment, the fluid layer undergoes heating from below and cooling at both the top

and one lateral side wall. The experiment revealed a typical flow structure, as depicted in Figure 3. The domain of the fluid can be divided into two distinct regions. Along the cooled side wall, a boundary layer was observed to descend along the wall and spread over the bottom as a cold tongue. On the other side, near the adiabatic wall, the flow pattern resembled observations made in turbulent RB convection cells. In addition to the BALI-metal experiment, there are also more recent experiments to investigate into the metallic layer, for example, HELM-LR focusing on low aspect ratios [4], HELM with an emphasis on high Rayleigh numbers [5].

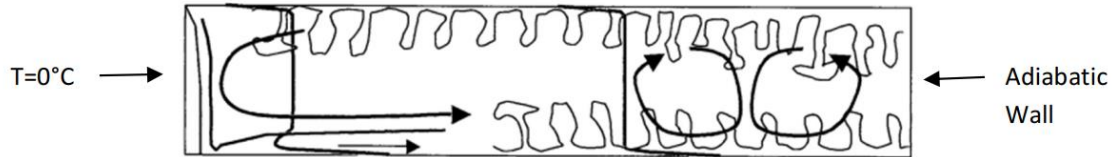


Figure 3 General observations of the fluid pattern in BALI-Metal experiment [2]

In recent years, there has been significant interest in the numerical simulation of the metallic layer in corium within the field of nuclear engineering and severe accident analysis, driven by development in computational technology. Numerical studies offer advantages such as flexibility, cost-effectiveness, and the ability to provide detailed insights into flow structure and heat transfer. Researchers have employed various computational fluid dynamics (CFD) techniques to investigate the thermo-fluid behavior and heat transfer characteristics of the metallic layer. However, modeling the turbulence in natural convection flow presents a challenge, and different approaches have been used, including Direct Numerical Simulation (DNS), Large Eddy Simulation (LES), and Reynolds-Averaged Navier-Stokes (RANS) models, in that order of least-to-most expensive and least-to-most accurate. While specific DNS studies focused on the metallic layer in corium are limited, valuable insights can be gained from related works. A summary of the numerical study of the turbulent RB convection can be found in a review study[6].

DNS, which resolves all scales of turbulent flow without relying on turbulence modeling, is a computationally intensive approach. While specific DNS studies focused on the metallic layer in corium are limited, valuable insights can be gained from related works. Paolucci, S. et al. presented 2D DNS simulations of turbulent natural convection in a rectangular enclosure[7]. Soria, M. et al. conducted a DNS simulation of natural convection in a tall cavity with Rayleigh number  $6.4 \times 10^8$  [8]. Prasopchingchana, U. et al. explores the behavior of turbulent natural convection in a square cavity with Rayleigh number up to  $10^9$ [9]. However, when it comes to the metallic fluid layer, the Rayleigh number can be higher, and the geometry of the system also has a crucial impact on the distribution of heat transfer. Thus, to obtain reference data and gain more detailed insights into the thermo-fluid behavior of the metallic layer, it is important to conduct DNS simulation. Additionally, the RANS method is commonly used in industrial practice as its low demand on computational effort. Comparing RANS models with experimental data is a conventional approach for assessment. However, a more comprehensive evaluation can be achieved by comparing them with DNS data, which provides detailed information on turbulence characteristics such as Reynolds stress, turbulent kinetic energy, and turbulent heat fluxes.

Therefore, in this study, a DNS analysis of turbulent natural convection based on the BALI-Metal 8U experiment is performed. The Rayleigh number is around  $2.16 \times 10^{10}$  and the Prandtl

number is 6.94. Three different RANS models (SST k- $\omega$ , standard k- $\epsilon$ , and Reynolds stress equation model (RSM)) are considered, and the simulation results are compared to the corresponding experimental data. The focus of the comparison lies on mean field quantities, including velocity, temperature, and heat flux, as well as turbulence quantities such as turbulent kinetic energy (TKE), and turbulent heat flux (THF).

In the rest of this paper, a comprehensive overview of the numerical model employed, including the governing equations and turbulence modeling, which will be discussed in Chapter 2. Chapter 3 will outline the numerical approach utilized in this study, including the problem setup and the meshing strategy implemented in the simulations. The obtained simulation results and their comparison with experimental data will be presented and thoroughly discussed in Chapter 4. Finally, Chapter 5 will conclude the paper and provide an outlook for future research.

## 2. Numerical model

### 2.1 Governing equations

When modeling natural convection, the incompressible Navier-Stokes equation incorporating the Oberbeck-Boussinesq approximation is commonly used[10], which assumes that the density variation only depends on the temperature change, such that

$$\frac{\rho - \rho_*}{\rho_*} = -\beta(T - T_*)$$

Therefore, the governing equations of the RBC flow is shown below:

$$\text{Mass } \nabla \cdot \mathbf{u} = 0$$

$$\text{Momentum } \frac{\partial \mathbf{u}}{\partial t} + \mathbf{u} \cdot \nabla \mathbf{u} = -\frac{1}{\rho_*} \nabla p + \nu \nabla^2 \mathbf{u} + g\beta(T - T_*)\vec{z}.$$

$$\text{Energy } \frac{\partial T}{\partial t} + \mathbf{u} \cdot \nabla T = k \nabla^2 T$$

where  $\mathbf{u} = (u, v, w)$ ,  $T$  and  $p$  denotes the velocity, temperature and pressure field, respectively. On the right-hand side of the momentum equation, the last term means the buoyancy effect induced by the temperature difference within the flow, which works on the vertical direction,  $z$ .

The equations can be normalized using the characteristic length  $l$  [m], a time scale  $\frac{l^2}{\alpha}$  [s] and a temperature scale  $\Delta = (T - T_*)$  [K] [10]. The dimensionless equations are

$$\text{Mass } \nabla \cdot \mathbf{u} = 0$$

$$\text{Momentum } \frac{\partial \mathbf{u}}{\partial t} + \mathbf{u} \cdot \nabla \mathbf{u} = -\nabla p + Pr \nabla^2 \mathbf{u} + RaPrT\vec{z}$$

$$\text{Energy } \frac{\partial T}{\partial t} + \mathbf{u} \cdot \nabla T = \nabla^2 T$$

There are two derived dimensionless numbers, Rayleigh and Prandtl numbers yield in the equations. The Rayleigh number ( $Ra = \frac{g\beta l^3 \Delta}{\alpha \nu}$ ) denotes the ratio of the fluid buoyancy force to the viscous force, which is also indicates the Rayleigh-Bénard instabilities. When the Rayleigh

number is larger than  $10^6$ , the RBC flow will become turbulent. The Prandtl number ( $Pr = \frac{\nu}{\alpha}$ ) represents the effect of the material of the fluid, denoting the ratio of the momentum diffusion to heat diffusion.

## 2.1 Turbulence modelling

As mentioned earlier, the flow within the metallic layer can exhibit fully turbulent behaviour due to the high Rayleigh number. To quantitatively analyse the turbulence, one can employ Reynolds decomposition of the governing equations. This involves decomposing a field variable into a mean value and a turbulent fluctuation value, such that

$$d = \bar{d} + d'$$

where  $\bar{d}$  is the temporal average of  $d$  and  $d'$  is the instant fluctuation with the property of  $\overline{d'} = 0$ . It should be noted that the property  $\overline{d'} = 0$  holds, indicating that the average of the fluctuation is zero. By employing this decomposition, the time-averaged characteristics of the natural convection flow can be described as follows:

Mass

$$\nabla \cdot \bar{\mathbf{u}} = 0$$

Momentum

$$\frac{\partial \bar{\mathbf{u}}}{\partial t} + \bar{\mathbf{u}} \cdot \nabla \bar{\mathbf{u}} = -\nabla \bar{p} + Pr \nabla^2 \bar{\mathbf{u}} - \nabla \overline{u_i' u_j'} + RaPr \bar{T} \vec{z}$$

Energy

$$\frac{\partial \bar{T}}{\partial t} + \bar{\mathbf{u}} \cdot \nabla \bar{T} = \nabla^2 \bar{T} - \nabla \overline{u_i' T'}$$

where  $\overline{u_i' u_j'}$  is called Reynolds stress, which denotes the impact from the turbulent fluctuation field to the mean flow field.  $\overline{u_i' T'}$  is called turbulent heat flux (THF), which denotes the impact from the turbulence to the mean temperature field.

Another important turbulent quantity of interest is the turbulent kinetic energy (TKE). TKE provides a measure of turbulence intensity within the flow. It can be defined as half of the sum of the squared fluctuations in the velocity components. Mathematically, the TKE is defined as:

$$k = \frac{1}{2} (u'u' + v'v' + w'w').$$

Based on the definition, one can also derive the transport equation of the TKE in the natural convection as shown below

$$\begin{aligned} \frac{\partial k}{\partial t} + \bar{u} \cdot \nabla k = & -\overline{u'_j u'_i} \frac{\partial \bar{u}_j}{\partial x_i} - Pr \overline{\left( \frac{\partial u'_j}{\partial x_i} \right)^2} + Ra Pr \overline{w' T'} \\ & + \frac{\partial}{\partial x_i} \left( Pr \overline{u'_j} \frac{\partial \bar{u}_j}{\partial x_i} - \frac{1}{2} \overline{u'_i u'_j u'_j} - \frac{1}{\rho} \overline{u'_i p'} \right) \end{aligned}$$

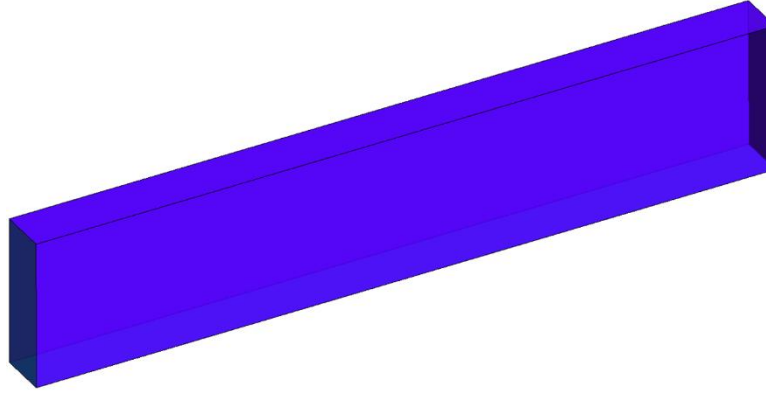
The transport equation for TKE can be further analyzed by examining its individual terms, which is also called TKE budget analysis. On the left-hand side, the first term represents the time derivative of TKE, while the second term represents the spatial advection. On the right-hand side, the equation includes several terms. The first term accounts for the production of TKE by shear forces within the flow. The second term represents the dissipation of TKE due to viscous effects. The third term  $Ra Pr \overline{w' T'}$ , corresponds to the production of TKE by the buoyancy force, which is an additional term when compared to the TKE budget in the absence of buoyancy forces. This term is proportional to the vertical component of the turbulent heat flux,  $\overline{w' T'}$ . The final term captures the spatial redistribution of TKE caused by viscous, turbulence, and pressure effects. By considering these terms, the TKE budget can provide insights into the balance and interplay of various forces influencing the turbulent behavior of the flow.

In RANS models, the governing equation for the mean fields is resolved, while the Reynolds stresses and turbulent heat fluxes are modeled [11]. Two commonly used models for turbulence modeling are the k- $\epsilon$  and k- $\omega$  models. The k- $\epsilon$  model focuses on modeling turbulent kinetic energy ( $k$ ) and dissipation rate of turbulence  $\epsilon$  [12]. It solves transport equations for  $k$  and  $\epsilon$ , considering their production, transport, and dissipation. The k- $\omega$  model is an improved version that addresses limitations of the k- $\epsilon$  model, particularly in regions with adverse pressure gradients and near-wall flows. It solves transport equations for  $k$  and  $\omega$ , where  $\omega$  represents the specific rate of dissipation. The k- $\omega$  SST model, a popular variant of the k- $\omega$  model, is commonly used due to its generality [13]. The k- $\omega$  SST model switches to the k- $\omega$  formulation, which allows for better prediction of boundary layer separation, transitional flows, and regions of adverse pressure gradients. In regions away from the wall it is reverted to the k- $\epsilon$  formulation to avoid the sensitivity of the k- $\omega$  model to the free-stream turbulence properties. Another commonly used turbulence model is the RSM, which directly solves transport equations for the individual components of Reynolds stresses, providing a detailed representation of the turbulence structure and accounting for anisotropy in turbulent flows [14].

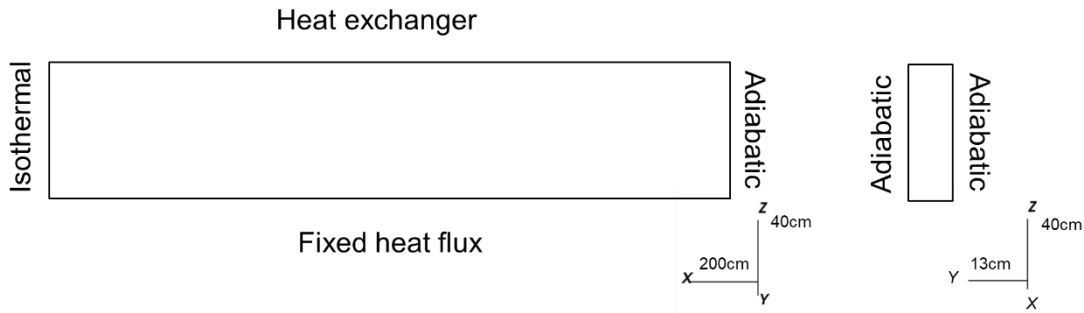
### 3. Numerical methods

#### 3.1 Problem description

As mentioned in Chapter 1, the simulations performed in this study are based on the BALI-Metal experiment 8U test [15]. The test geometry is described in Figure 4. The test section is rectangular, 13cm in width along y-direction, 200cm in length along x-direction and 40cm in height along the axis z.



(a) 3D test section



(b) Front view and the left view of the domain with the thermal boundary conditions

Figure 4 Schematic of BALI-Metal experiments

The experiment utilizes water as the simulant, with the test section being heated uniformly from the bottom by fixed power input. To simulate the radiation heat transfer that occurs in an actual reactor, a heat exchanger is placed on the top surface[16]. The front, back, and the right lateral side wall were treated as adiabatic walls, while the left lateral side had an isothermal boundary condition achieved by cooling the water, resulting in the formation of a thin ice layer with a negligible thickness compared to the overall geometry. A summary of the simulation parameters can be found in Table 2. It should be noted that the power input in the experiment is 2000W, but only 86% are measured at the heat removal surfaces, which means there is still heat loss from the other boundaries. So, the power input on the bottom in this study is set to 86% of the original value, resulting in 1680  $W$ . The heat transfer coefficient  $h$  on the top wall is also adjusted from  $100 \frac{W}{m^2 \cdot K}$  to  $113 \frac{W}{m^2 \cdot K}$  according to the calibration.

Table 1 Simulation parameters

Rayleigh number	$2.16 \times 10^{10}$
Prandtl number	6.94
Kinetic boundary condition	No-slip walls

Heat exchanger on the top wall	$h = 113 \frac{W}{m^2 \cdot K}, T_{inf} = 0^\circ C$
Temperature on the left lateral wall	$T_{left} = 0^\circ C$
Power input on the bottom	$Q_{bottom} = 1680W$

Four simulation cases will be performed, including one case using DNS and three cases using RANS models. The RANS cases employ different turbulence models: SST k- $\omega$ , Standard k- $\epsilon$ , and RSM (see Table 2). The DNS case is solved using the Nek5000 open-source CFD code, which utilizes the Spectral Element Method (SEM) discretization scheme[17]. On the other hand, the RANS cases are simulated using Ansys Fluent, based on the Finite Volume Method (FVM).

Table 2 Simulation cases

Case number	Turbulence model	Software
Case 1	DNS method	Nek5000 v19.0
Case 2	SST k- $\omega$	Ansys Fluent v21.2
Case 3	Standard k- $\epsilon$	Ansys Fluent v21.2
Case 4	RSM	Ansys Fluent v21.2

## 3.2 Mesh requirement

### 3.2.1 DNS

Since DNS resolves all scales of turbulence, the mesh for a DNS simulation should consider the smallest dissipation scale. Grossman and Lohse proposed a scaling theory of the natural convection, which can give a pre-estimation of the Reynolds number  $Re$  and Nusselt number  $Nu$  based on the  $Ra$  and  $Pr$  [18]. Shishkina et al. derived the formulas to calculate the mesh requirements of the turbulent natural convection flow[19]. Bian B. et al. added a post-check method of DNS mesh and established a pipeline (see Figure 5) to generate the DNS mesh based on an internal heated natural convection problem[20]. In the pipeline, the boundary layer thickness should be identified first using the scaling theory, then one can estimate the mesh size in both the bulk domain and the boundary layers using Shishkina et al.'s formulas. Based on the pre-estimation results, the mesh can be constructed. However, the mesh should also be post-verified using the simulation result of the dissipation length scale to ensure that it satisfies the requirement of the DNS.



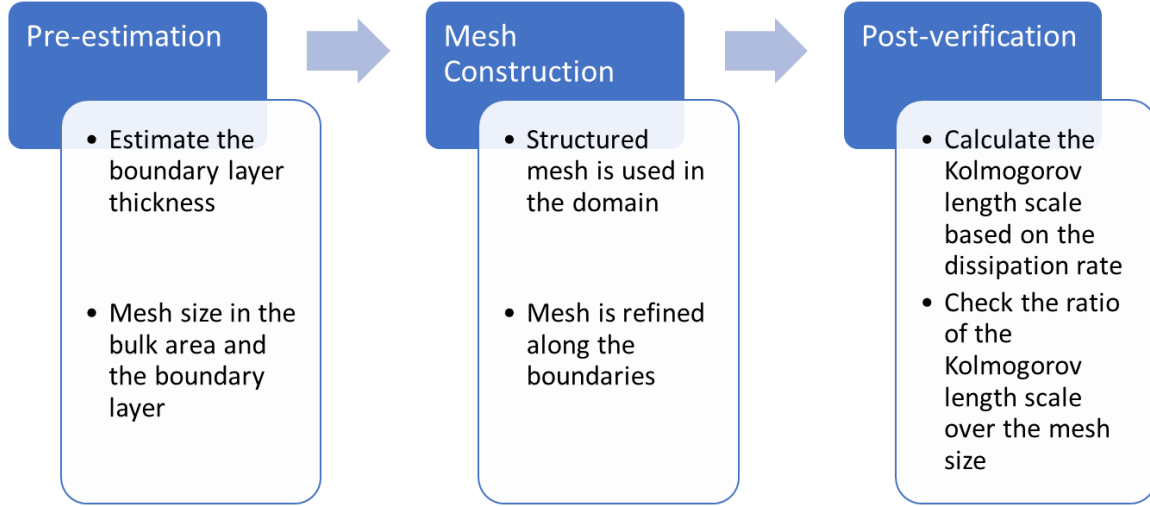


Figure 5 Workflow of the DNS mesh construction in natural convection flow simulation

Grossman and Lohse developed a scaling theory that utilizes a Ra-Pr phase-diagram method to estimate the boundary layer thickness in natural convection over a wide range of Ra and Pr [18]. Similar to forced convection flows, the kinetic boundary layer thickness and thermal boundary layer thickness can be estimated by considering the Re and Nu, respectively. These two numbers can be approximated based on the values of Ra and Pr for the flow.

$$Re = C_1 Ra^{a1} Pr^{b1}$$

$$Nu = C_2 Ra^{a2} Pr^{b2}$$

The boundary layer thicknesses for the kinetic boundary layer  $\lambda_u$  and thermal boundary layer  $\lambda_\theta$  can be estimated, using

$$\lambda_u = \frac{L}{4\sqrt{Re}}$$

$$\lambda_\theta = \frac{L}{2Nu}.$$

The power coefficients are determined based on Ra-Pr regime. In the present study, the Ra is  $2.16 \times 10^{10}$  and the Pr is 6.94. The corresponding Re, Nu,  $\lambda_u$  and  $\lambda_\theta$  can be estimated as follows:

$$Re = 0.088 Ra^{4/9} Pr^{-2/3} = 946.65$$

$$Nu = 0.05 Ra^{1/3} = 139.17$$

$$\lambda_u = \frac{L}{4\sqrt{Re}} = 0.325 \text{ cm}$$

$$\lambda_\theta = \frac{L}{2Nu} = 0.144 \text{ cm}$$

After that, the mesh size within the boundary layer and the bulk flow can be calculated using Shishkina et al.'s formulas which are derived based on the dissipation analysis of the natural convection [19].

$$h^{BL} \leq \begin{cases} 2^{-\frac{3}{2}} a^{-1} Nu^{-\frac{3}{2}} Pr^{\frac{3}{4}} A^{-\frac{3}{2}} \pi^{-\frac{3}{4}} L, & Pr < 3 \times 10^{-4}, \\ 2^{-\frac{3}{2}} a^{-1} Nu^{-\frac{3}{2}} Pr^{0.5355-0.033 \log Pr} L, & 3 \times 10^{-4} \leq Pr < 1, \\ 2^{-\frac{3}{2}} a^{-1} Nu^{-\frac{3}{2}} Pr^{0.0355-0.033 \log Pr} L, & 1 \leq Pr < 3, \\ 2^{-\frac{3}{2}} a^{-1} E^{-\frac{3}{2}} Nu^{-\frac{3}{2}} L, & Pr \geq 3, \end{cases}$$

$$h^{bulk} \leq \begin{cases} \frac{Pr^{\frac{1}{2}}}{Ra^{\frac{1}{4}}(Nu-1)^{\frac{1}{4}}}, & Pr \leq 1, \\ \frac{1}{Ra^{\frac{1}{4}}(Nu-1)^{\frac{1}{4}}}, & Pr > 1 \end{cases}$$

where  $a \approx 0.482$ ,  $A \approx 0.332$ ,  $E \approx 0.982$ , and  $L$  is the characteristic length.

Incorporating the  $Re$  and  $Nu$  into the formulas, we obtain

$$h^{BL} \leq 0.0177 \text{ cm}$$

$$h^{bulk} \leq 0.0304 \text{ cm}$$

In the SEM method employed by Nek5000, the mesh consists of collocation grid points within each element[21]. It is the size between these grid points that needs to satisfy the mesh requirements. Consequently, the DNS case requires approximately 200,000 elements in the mesh. Figure 4 illustrates the mesh on the middle plane, highlighting the refined mesh along the boundaries. The SEM utilizes a polynomial order of 7, resulting in a total of 102 million grid points in the entire domain. In the post-check, the ratio between the Batchelor scale and the mesh size is calculated, and a histogram of the ration distribution on the XZ-middle surface is shown in Figure 6. All the value are larger than 1, which means the mesh size is smaller than the smaller dissipation length scale.

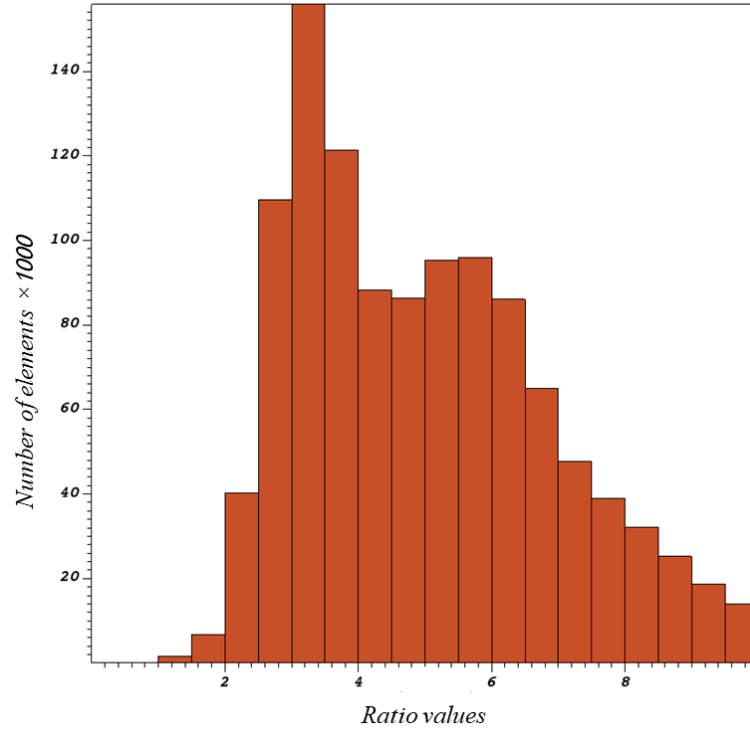


Figure 6 Ratio distribution between the Batchelor length and the mesh cell size.

### 3.2.2 RANS

In the preceding section, we determined the thickness of the boundary layer, which is an important consideration in the RANS calculation. As a result, we refined the mesh in the vicinity of the bottom, left, and top boundaries. The distribution of cells on the XZ middle slice ( $y=6.5\text{cm}$ ) is depicted in Figure 7.

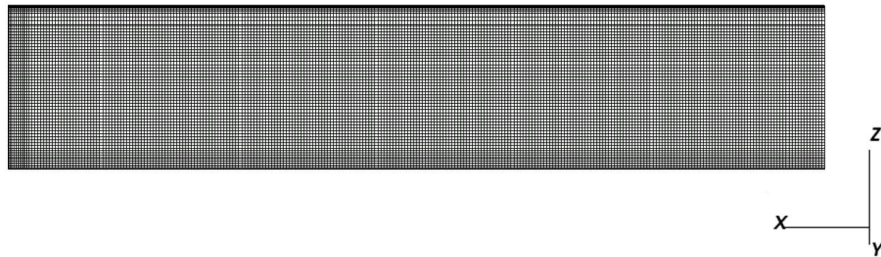


Figure 7 RANS mesh on the XZ middle slice ( $y=6.5\text{ cm}$ )

In this study, we conducted a mesh sensitivity analysis for the RANS calculation using three different mesh sizes (see Table 3). For the sake of brevity and simplicity, we present only the numerical results obtained with the  $k-\omega$  SST turbulence model, as similar results were obtained with other turbulence models investigated in this study. We compared the temperature profile along the  $x$  direction at the middle ( $z=20\text{cm}$ ) of the XZ middle slice, as well as the heat flux profile along the  $z$  direction on the left ( $x=0\text{cm}$ ) of the XZ middle slice. Figure 8 illustrates the comparison of the temperature and heat flux calculated using each mesh. It is shown that mesh independence is achieved after one refinement. Specifically, Mesh 2 provided satisfactory

results without further refinement, indicating mesh independence. Therefore, Mesh 2 was chosen for the present study, and the following RANS results were obtained using this computational mesh.

Table 3 Meshes for sensitivity study

Mesh number	Size
Mesh1	~200K
Mesh2	~500K
Mesh3	~1M

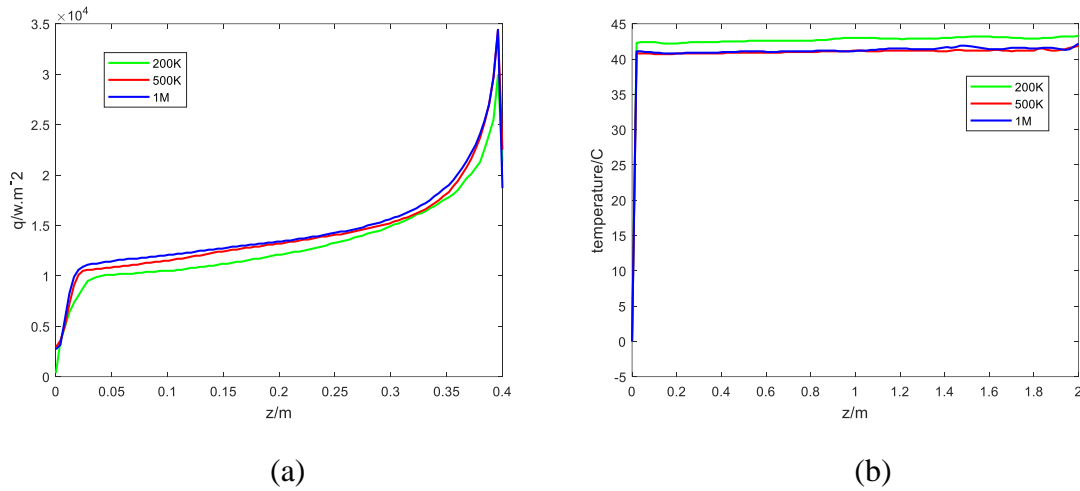
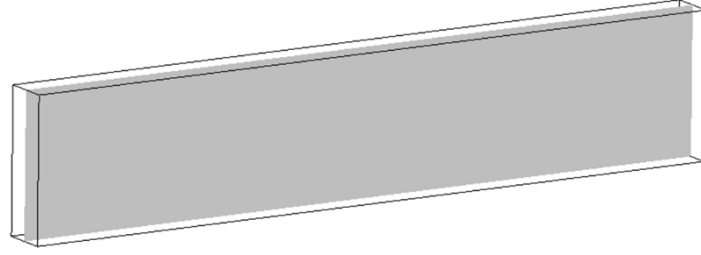


Figure 8 Comparison values for the mesh sensitivity study (a) Temperature profile along the x direction at the middle ( $z=20$ cm) of the XZ middle slice. (b) Teat flux profile along the z direction on the left ( $x=0$ cm) of the XZ middle slice.

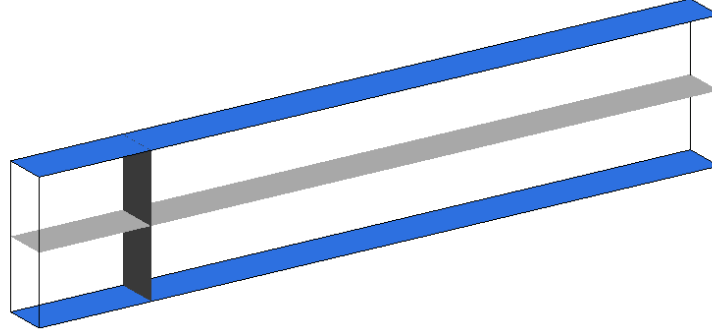
#### 4. Results and discussion

In this chapter, we present the simulation results and compare them with the experimental data. The DNS case is performed on the High-Performance Computing (HPC) cluster Vega [22], utilizing approximately 2000 MPI ranks and consuming around 1 M core-hours. A quasi-steady state is achieved in the simulation, where the quantities exhibit oscillations within a specific range. During this quasi-steady state, time-average is applied to generate the mean field and turbulent quantities. In the RANS simulations, a transient solution is employed, utilizing the unsteady RANS (URANS) method. The results are further postprocessed once the simulations reach the quasi-steady state.

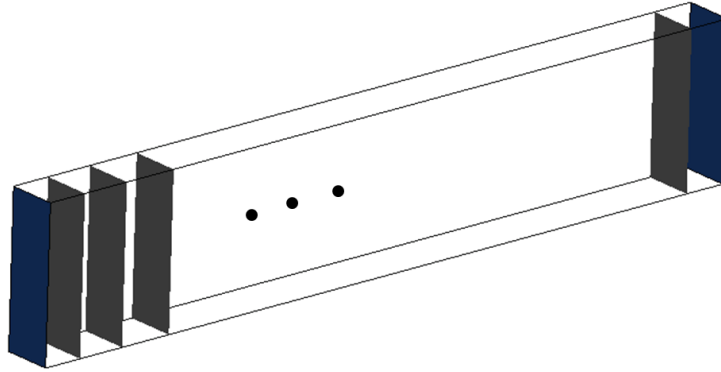
In the following of this chapter, the simulation result on different locations in the 3D domain will be presented. The locations are defined in Figure 9, including a XY-middle slice ( $y=6.5$  cm) of the geometry, the planes where the temperature data was measured in the BALI-Metal experiment (Figure 9 (b)), and 50 uniformly distributed YZ-planes for illustrating the quantity distribution along the horizontal direction,  $x$ .



(a) XY-middle slice ( $y=6.5$  cm)



(b) Measurement locations of the temperature in the BALI-Metal experiment: Bottom boundary, top boundary, a XY middle plane ( $z=20$ cm) and a YX plane ( $x=33$ cm).



(c) 50 uniformly distributed YZ-planes

Figure 9 Locations of the post-processing

#### 4.1 Velocity field

Figure 10 depicts the instantaneous velocity distribution on the middle XZ plane ( $y=6.5$ cm) of the DNS case (Case 1). The flow exhibits intensive turbulence, capturing turbulent eddies of varying sizes throughout the domain, particularly near the boundaries. The observed flow pattern is in good consistent with the general flow structure observed in the BALI-Metal experiment. The domain can be divided into two distinct regions. In the left part, a large-scale

flow circulation is evident. The descending flow near the left lateral cooling wall is captured. Additionally, the formation of a "cold tongue" originating from the left corner is also observed, penetrating towards the right side. Meanwhile, a RBC cell is observed in the right part of the domain. The flow structure in the middle region experiences the combined effects of buoyancy in the vertical direction, leading to the formation of RBC cells, and the influence of large-scale circulation driven by shear forces. Close to the bottom wall, the velocity of the large-scale circulation is relatively high, indicating a stronger shear force effect. Conversely, near the top wall, the velocity is comparatively lower, resulting in a larger buoyancy effect and the generation of multiple turbulent vortices.

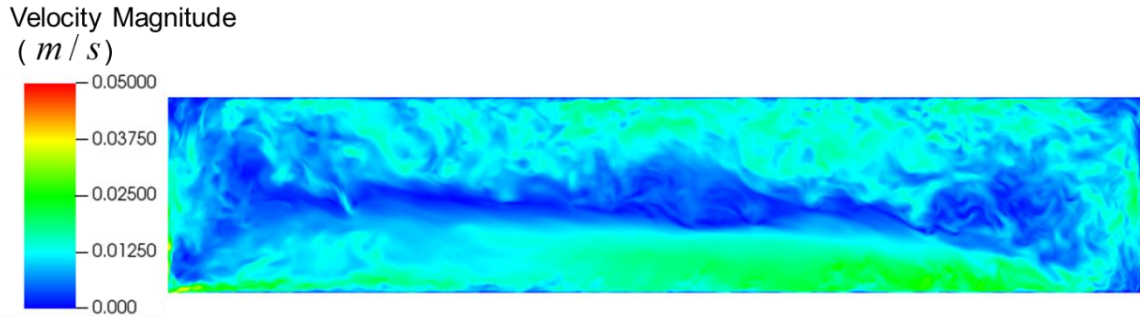


Figure 10 Instantaneous velocity distribution on the XZ-middle slice ( $y=6.5\text{cm}$ ) in Case 1.

The mean velocity field obtained from the DNS simulation (Case 1) is analyzed. Figure 11 presents a comparison of the mean velocity on the XZ-middle plane ( $y=6.5\text{cm}$ ). The results demonstrate that both the  $k-\omega$  SST model (Case 2) and the  $k-\epsilon$  model (Case 3) are capable of reproducing the rotating buoyancy cell (RBC) in the right part of the domain. However, the RSM model (Case 4) only captures the presence of the large-scale circulation. When compared to the DNS results, it can be observed that the  $k-\omega$  SST model is able to provide a similar flow pattern, indicating its capability in capturing the flow behavior.

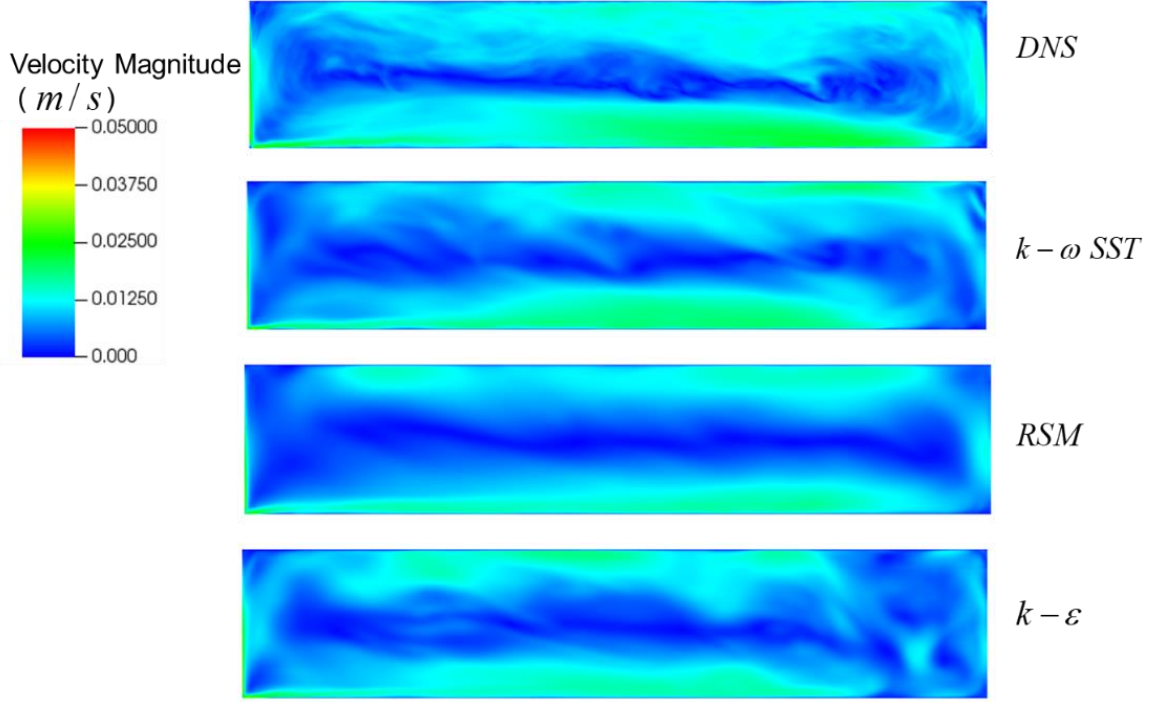


Figure 11 Mean velocity distribution on the XZ-middle slice ( $y=6.5\text{cm}$ ) in 4 cases.

The TKE of the turbulence flow in the simulations is also obtained and compared. To analyze the distribution of TKE in different cases and illustrate the turbulent intensity throughout the domain, we employ 50 uniformly distributed YZ planes along the x direction, as depicted in Figure 9 (c). The TKE is averaged on each plane, allowing us to obtain a planar-averaged TKE profile along the x direction. Figure 12 presents the TKE profiles for the different cases. In the DNS simulation (Case 1) profile, the TKE exhibits high values near the side walls and reaches its peak within the RBC zone. Among the RANS cases, the  $k-\omega$  SST model (Case 2) reproduces a similar profile to Case 1, because the flow structure is similar between Case 1 and Case 2. But it underestimates the peak values near the side walls. The  $k-\epsilon$  model (Case 3) exhibits a TKE value similar to Case 1 near the left cooling boundary ( $x=0\text{cm}$ ), but it overpredicts the TKE peak within the RBC zone. On the other hand, the RSM model overpredicts the TKE values throughout the entire domain.

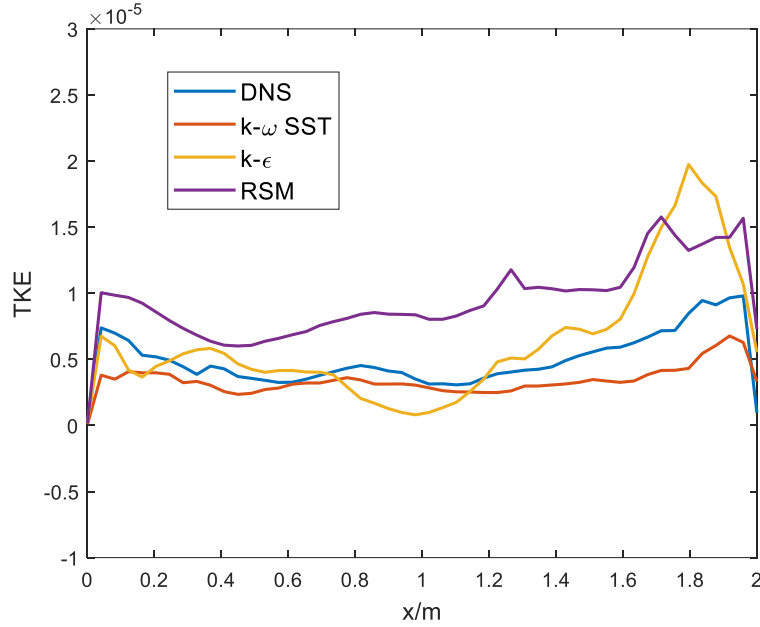


Figure 12 Plane-averaged TKE profiles along the x direction in 4 cases.

## 4.2 Temperature field

Figure 13 depicts the instantaneous temperature distribution on the XZ-middle slice ( $y=6.5\text{cm}$ ) using six isothermal levels. The influence of turbulence mixing is evident as the temperature in the bulk flow tends to become more uniform, with an average temperature of approximately 37 degrees. The presence of a "cold tongue" near the left bottom heat plate is clearly outlined, accompanied by thermal penetration along the bottom wall. Furthermore, thermal plumes can be observed emanating from the top cooling boundaries. In order to compare the temperature distribution on the bottom heating plate, the results of the four simulations are presented in Figure 14. It is evident that the DNS case (Case 1) exhibits lower temperatures compared to the RANS cases. Striped structures are observed in all cases, resulting from the vortices above



the plate. In addition, the DNS case demonstrates a stronger thermal penetration associated with the "cold tongue."

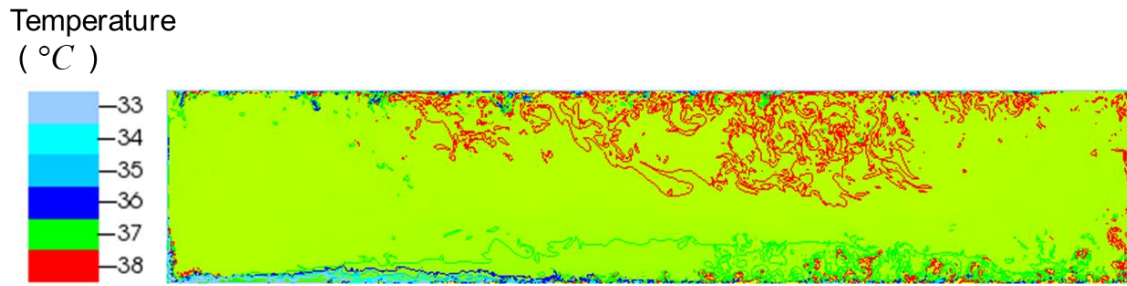


Figure 13 Instantaneous temperature distribution with isothermal lines on the XZ-middle slice (y=6.5cm) in the DNS case (Case 1) .

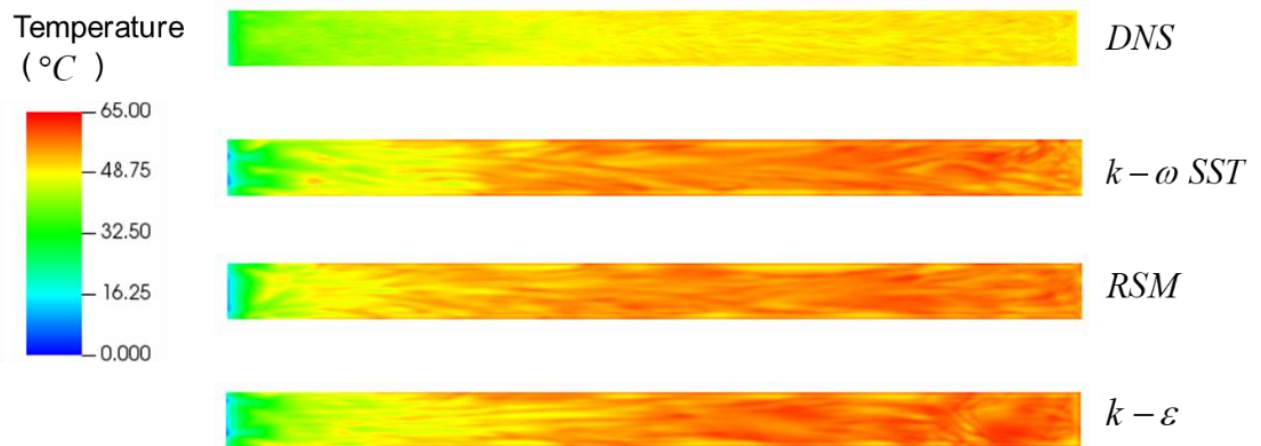
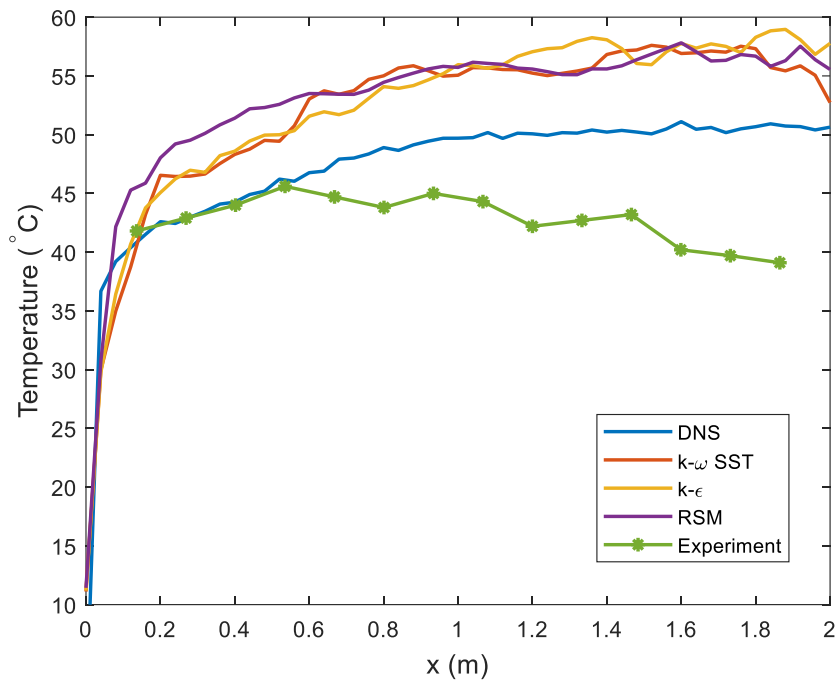


Figure 14 Mean velocity distribution on the bottom in 4 cases

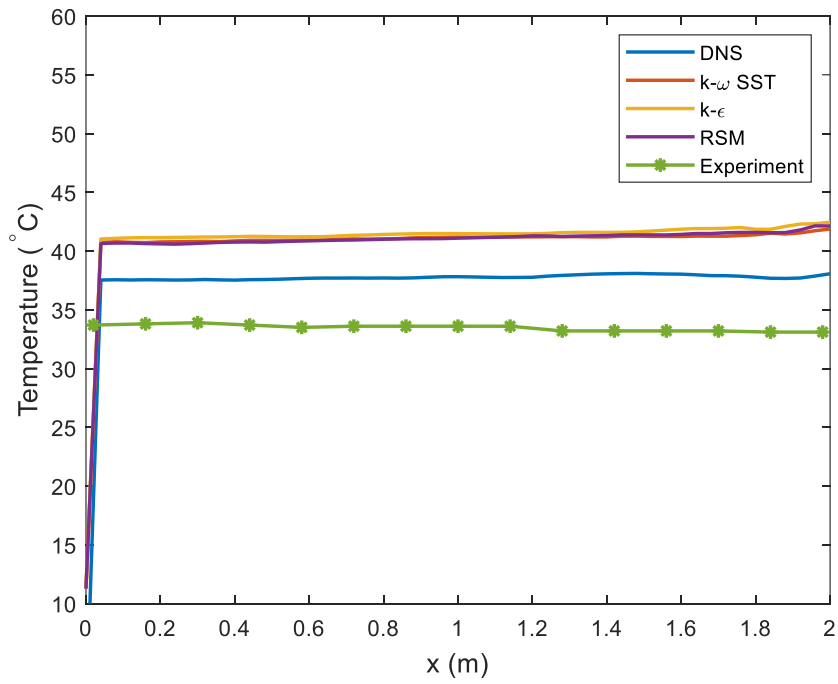
In the experimental setup, temperature measurements were done at various locations, including the bottom heating plate, the top cooling surface, a horizontal middle plate within the test section, and a vertical plate positioned 33cm away from the lateral cooling wall (see Figure 9 (b)). Similarly, temperature values were extracted from the simulations at these corresponding locations, and a comparison result is presented in Figure 15 Temperature comparison between the simulation results and the experimental data. It is important to note that each temperature value on the plots from the simulations represents the average temperature along the y-direction, obtained by averaging 13 point values.

On the bottom heating plate, the DNS case shows good agreement with the experimental data close to the cooling lateral wall ( $x < 50\text{cm}$ ). However, it gradually overpredicts the temperature as the distance increases, resulting in a growing gap. The RANS cases consistently overpredict the temperature across the entire domain, deviating from both the experimental data and the DNS case. On the middle plate, where the temperature tends to become more homogeneous due to mixing effects, all cases, including the experimental data, show relatively flat

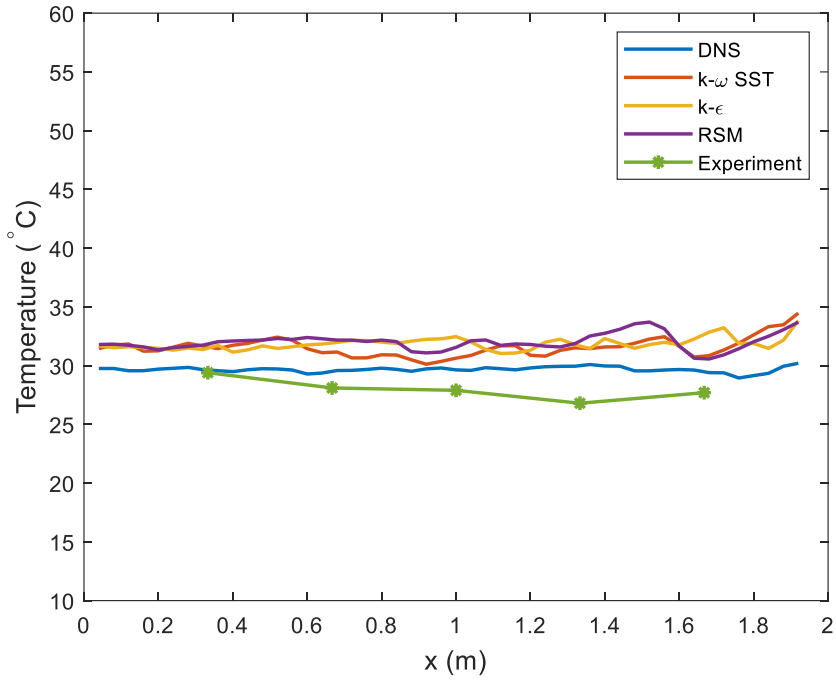
temperature profiles. However, all simulation cases overpredict the temperature compared to the experiment, with the DNS case providing the closest match to the profile. Moving to the top cooling plate, the difference between the simulation results and the experimental data becomes smaller, although the RANS cases still tend to slightly overpredict the temperature. When examining the comparison results on the vertical plane, all cases overpredict the temperature, but the DNS data exhibits closer agreement. Furthermore, in the DNS case, the temperature difference between the bottom and the bulk region aligns with the experimentally observed data. The peak near the bottom in all the simulation cases indicates the presence of the "cold tongue" effect.



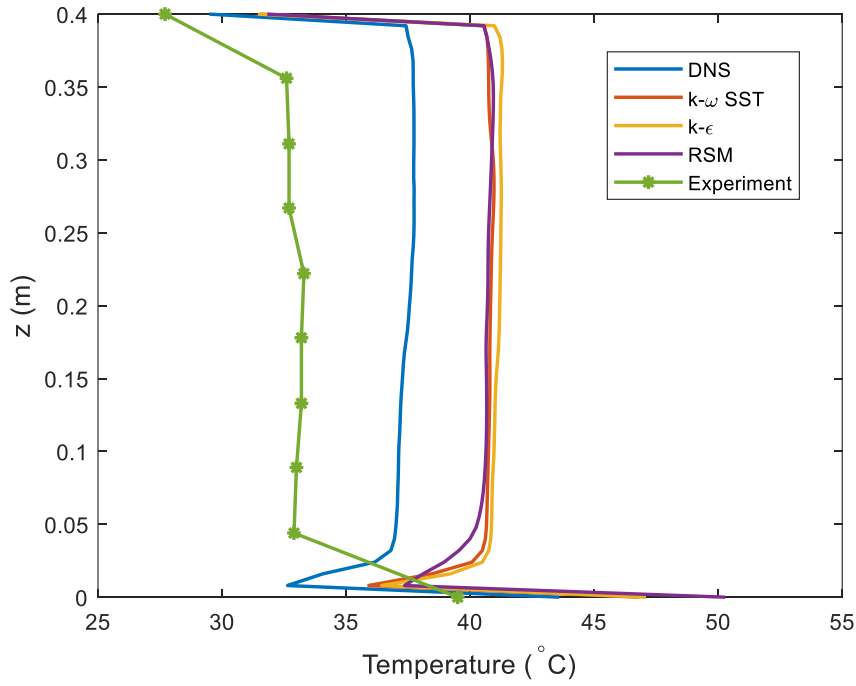
(a) Bottom ( $z=0\text{cm}$ )



(b) Middle ( $z=0.2\text{m}$ )



(c)Top (z=0.4m)



(d) vertical plane (x=0.33m)

Figure 15 Temperature comparison between the simulation results and the experimental data

In addition to studying the temperature field, we have also investigated the turbulent heat flux (THF) in the simulations. In RANS models, the THF is modeled using the Spalart-Allmaras

Generalized Differential Hypothesis (SGDH) approach[23], which considers turbulent viscosity  $\mu_t$ , turbulent Prandtl number  $Pr_t$ , and temperature gradient  $\nabla T$ , such that

$$\overline{u_i T'} = \frac{\mu_t}{Pr_t} \nabla T$$

The THF terms not only impact the mean temperature field but also influence the turbulent kinetic energy (TKE) production through the vertical THF  $\overline{w T'}$ , which is associated with buoyancy effects in natural convection flows. Figure 16 Comparison results of  $\overline{w T'}$  along the x-direction presents the comparison results of  $\overline{w T'}$  along the x-direction, where the values are planar-averaged across 50 uniformly distributed planes depicted in Figure. It can be observed that the k- $\omega$  SST is not capable of modeling the THF throughout the domain. The k- $\epsilon$  and RSM models are able to reproduce similar  $\overline{w T'}$  profiles as the DNS simulation near the left boundary ( $x < 30\text{cm}$ ). However, beyond that point, significant deviations become apparent.

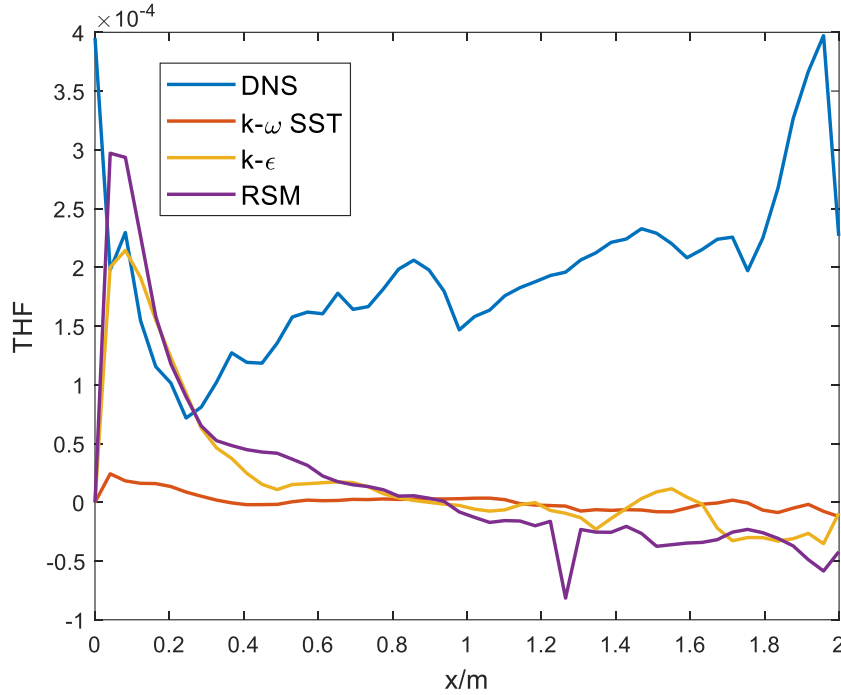


Figure 16 Comparison results of  $\overline{w T'}$  along the x-direction

### 4.3 Heat flux

The simulation also includes the analysis of heat flux distribution on the cooling boundaries. Figure 17 illustrates the mean heat flux field distribution on the lateral cooling wall. It is evident that the highest mean heat flux is observed near the top of the wall across all simulation cases, while a low heat flux region is present near the bottom. In the DNS case, the heat flux decreases from the bottom towards the middle and then increases after that. Conversely, in the RANS

cases, the heat flux shows an increasing trend from the bottom to the top. In the experimental setup, the heat flux profile along a vertical line in the middle of the lateral cooling wall was measured. Figure 18 provides a comparison of the heat flux profiles between the simulation results and the experimental data. It is shown that the DNS case successfully reproduces a similar heat flux profile to the experimental result. The heat flux initially increases from the bottom, and then decreases after it reaches a peak. In the middle part of the wall, it increases again towards the top. In contrast, the RANS cases reproduce the peak value close to the top but only exhibit a monotonically increasing heat flux trend.

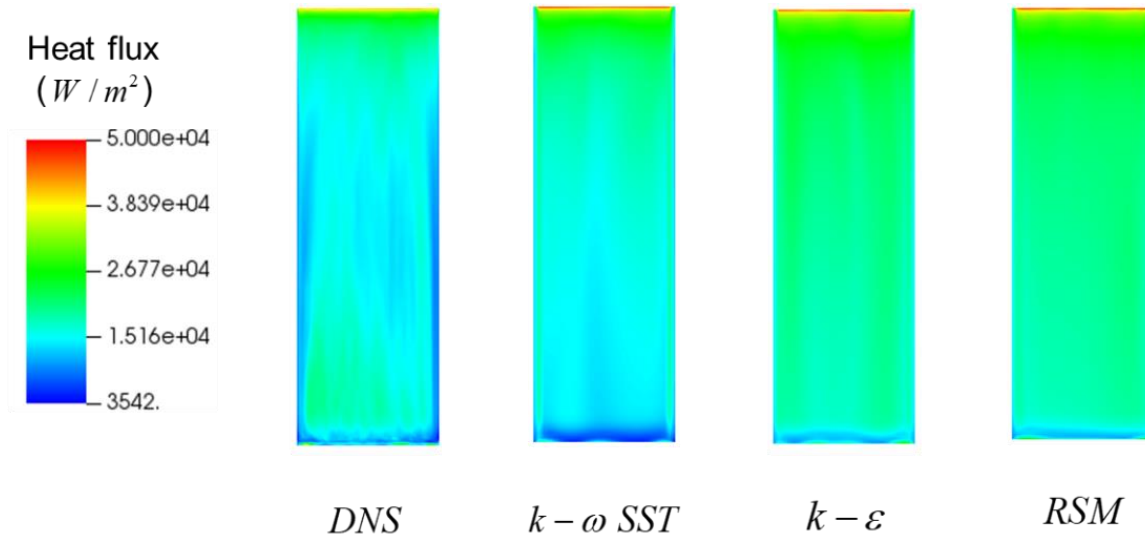


Figure 17 Mean heat flux distribution on the lateral cooling wall

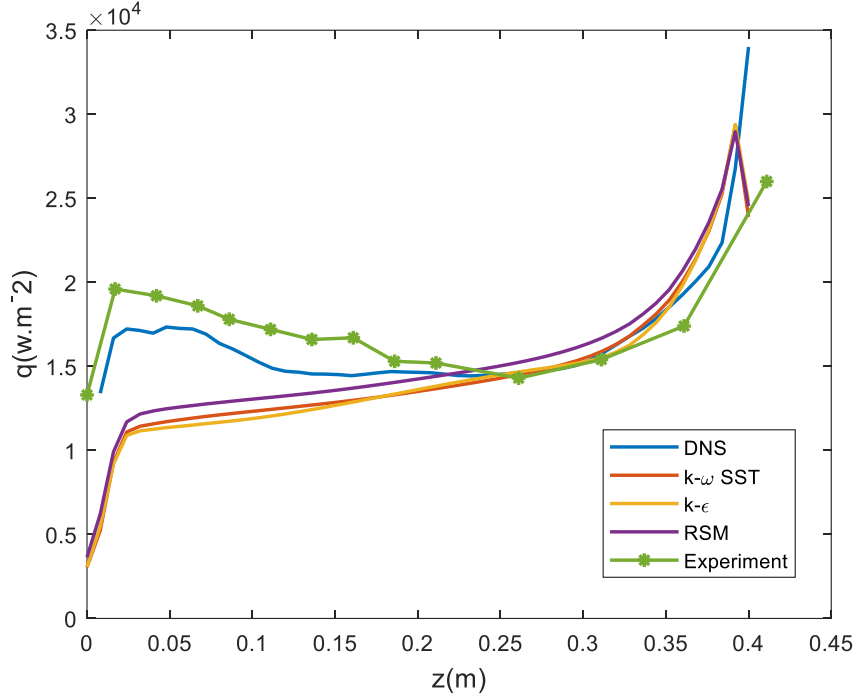


Figure 18 Heat flux profiles along the measurement line on the lateral cooling wall.

The increase in heat flux in the lower part of the wall is of interest to the focusing effect. This can be better understood by analyzing the instantaneous heat flux distribution on the lateral wall, as depicted in Figure 19. The distribution reveals that heat transfer is more stable in the upper part of the wall, while it shows fluctuations in the lower part due to the presence of turbulent eddies in that region. Additionally, small red areas are observed in the lower part of the wall at various recording times, indicating localized heat flux peaks that change their locations over time. It's important to note that Figure 17 and Figure 18 only display the time-averaged heat flux profile, resulting in the suppression of those peak values in the lower part of the wall. Nevertheless, these peaks still exist as relatively high values in the mean profile. However, the transient behavior plays a crucial role in the analysis of the focusing effect. For instance, we captured the transient maximum heat flux value during a 25-second period in the quasi-steady state of the DNS simulation, as depicted in Figure 20. It becomes evident that the maximum value of the instantaneous heat flux greatly exceeds that of the mean field. Such transient phenomena cannot be captured in the RANS cases.

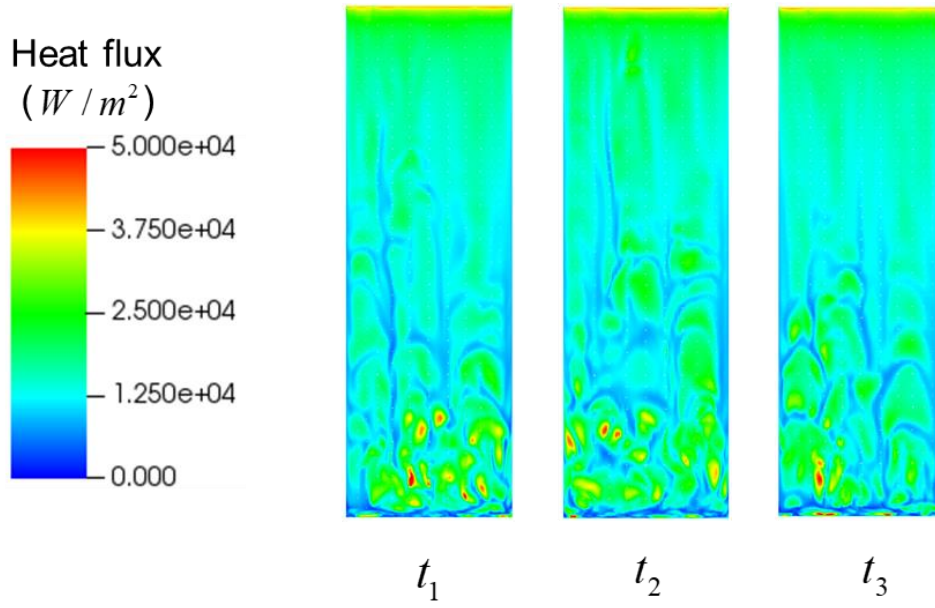


Figure 19 Instantaneous heat flux distribution on the lateral wall at different times in the DNS case

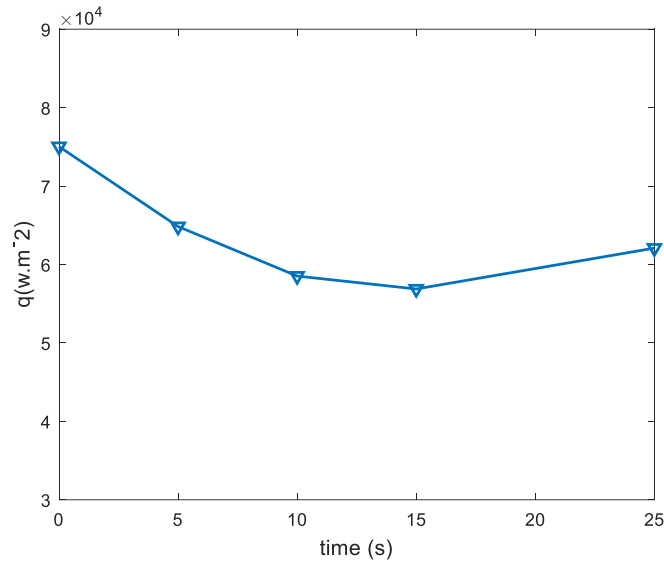


Figure 20 Maximum heat flux value during a 25-second period in the DNS case

The simulations also provide the mean heat transfer profile along the x-direction on the top cooling surface, which is then compared with the experimental data in Figure 21. The profile demonstrates oscillations in all simulations due to the presence of turbulent eddies near the top wall. In comparison to the RANS cases, the DNS simulation generates a more stable profile.

Utilizing the heat transfer distribution on the cooling surfaces, we calculated the spatially averaged heat flux on the boundaries and analyzed the energy balance in the domain, as shown in Table 4. The results reveal that the DNS case (Case 1) accurately predicts the energy balance when compared to the RANS cases. The average heat flux on the lateral wall serves as an



indicator of the strength of the focusing effect. The DNS result provides a reasonable value for this value, while the RANS case underpredicts the lateral heat flux.

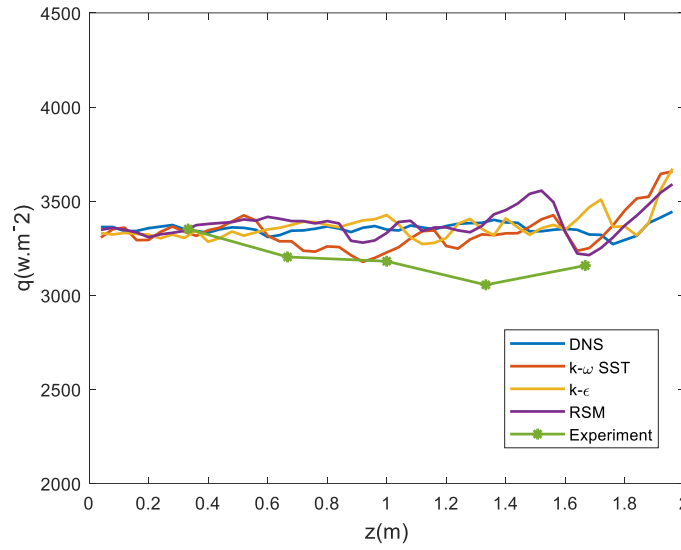


Figure 21 Heat flux profiles along x-direction on the top cooling wall.

Table 4 Average heat flux distribution and total energy balance

Case number	$q_{lateral}(W/cm^2)$	Percentage of $q_{lateral}$	$q_{Top}(W/cm^2)$	Percentage of $q_{Top}$
Case 1	1.6181	50.04%	0.3231	49.96%
Case 2	1.5388	47.45%	0.3409	52.55%
Case 3	1.5139	46.81%	0.3440	53.19%
Case 4	1.5087	46.65%	0.3451	53.35%
Experiment	1.66	50.92%	0.32	49.08%

## 5. Conclusions

This study focused on numerically simulating turbulent natural convection flow in a 3D fluid layer based on the BALI-Metal 8U experiment. The fluid layer undergoes heating from the bottom, and cooling at both the top surface and the left lateral wall. The Rayleigh number is around  $2.16 \times 10^{10}$  and the Prandtl number is 6.94. Different turbulent modelling methods were employed, including DNS and three RANS models: k- $\omega$  SST, standard k- $\epsilon$ , and RSM. The simulation results were also compared with experimental data, and the performance of the RANS models was evaluated using the DNS results as a reference.

The findings of this study revealed that DNS reproduced a two-distinct region flow structure that is consistent with the experimental observations. Specifically, a large flow circulation is observed in the left part of the domain, including the descending flow and the “cold tongue” along the bottom plate, while a RBC cell is captured in the right part of the domain. In addition, the k- $\omega$  SST model exhibited flow patterns and TKE profiles similar to those obtained from DNS simulations.

With respect to the temperature field, it tends to be homogenous in all simulations due to the mixing effect of the turbulence. The “cold tongue” originated from the lateral cooling wall caused a thermal penetration above the bottom heating plate. It was observed that all the simulations, including DNS, tended to overpredict the temperature field compared to the experimental data at the measurement locations. Nevertheless, DNS provided the closest results to the experimental data in terms of temperature. Furthermore, the analysis of turbulent heat flux (THF) demonstrated that the RANS models were inadequate in accurately modeling THF in turbulent natural convection flow based on SGDH approach.

The heat flux analysis showed that DNS successfully achieved good agreement with the experimental data in terms of heat flux distribution and energy balance, while the RANS models underestimated the lateral heat flux and overestimated the heat flux on the top surface. In another word, the focusing effect was underestimated in the RANS simulations. In addition, the transient maximum heat flux on the lateral cooling wall in the DNS simulation is captured, which was higher than the time-averaged value. This transient behavior can play a crucial role in estimating the focusing effect accurately.

## Funding

The authors would like to acknowledge the funding support from EU-IVMR (Project No. 662157). Boshen Bian appreciates the PhD scholarship from China Scholarship Centre (CSC).

## References

1. Komlev, A., et al., *Final report on stratified molten pool of simulant materials*. EC-H2020 IVMR Project, 2019. **No. 662157**.
2. Sehgal, B.R., et al., *Assessment of reactor vessel integrity (ARVI)*. Nuclear Engineering and Design, 2003. **221**(1): p. 23-53.
3. Bernaz, L., et al., *Thermalhydraulic phenomena in corium pools: numerical simulation with TOLBIAC and experimental validation with BALI*. 1999.
4. Li, Z., et al., *Experimental investigation on vertical heat transfer characteristics of light metallic layer with low aspect ratio*. Nuclear Engineering and Design, 2021. **377**: p. 111153.
5. Ma, L., et al., *Turbulent convection experiment at high Rayleigh number to support CAP1400 IVR strategy*. Nuclear Engineering and Design, 2015. **292**: p. 69-75.
6. Miroshnichenko, I.V. and M.A. Sheremet, *Turbulent natural convection heat transfer in rectangular enclosures using experimental and numerical approaches: A review*. Renewable and Sustainable Energy Reviews, 2018. **82**: p. 40-59.
7. Paolucci, S., *Direct numerical simulation of two-dimensional turbulent natural convection in an enclosed cavity*. Journal of Fluid Mechanics, 1990. **215**: p. 229-262.

8. Soria, M., et al., - *Direct Numerical Simulation of Turbulent Natural Convection Flows Using PC Clusters*, in *Parallel Computational Fluid Dynamics 2003*, A. Ecer, et al., Editors. 2004, Elsevier: Amsterdam. p. 481-488.
9. Prasopchingchana, U., *Direct numerical simulation of natural convection in a square cavity at high Rayleigh numbers via the Lagrange interpolating polynomial scheme*. International Journal of Thermal Sciences, 2022. **172**: p. 107276.
10. Goluskin, D., *Internally Heated Convection and Rayleigh-Bénard Convection*. 1st ed. 2016. ed. SpringerBriefs in Thermal Engineering and Applied Science. 2016, Cham: Springer International Publishing.
11. Wilcox, D.C., *Turbulence modeling for CFD*. 1993, La C nada, Calif: DCW Industries, Inc.
12. Launder, B.E. and D.B. Spalding, *The numerical computation of turbulent flows*. Computer Methods in Applied Mechanics and Engineering, 1974. **3**(2): p. 269-289.
13. Menter, F.R., *Two-equation eddy-viscosity turbulence models for engineering applications*. AIAA journal, 1994. **32**(8): p. 1598-1605.
14. Speziale, C.G., *Analytical Methods for the Development of Reynolds-Stress Closures in Turbulence*. Annual Review of Fluid Mechanics, 1991. **23**(1): p. 107-157.
15. N. Seiler, A.D., B. Bian, W. Villanueva, Y. Vorobyov, O. Zhabin, M. Kratochvil, L. Vyskocil. *CFD SIMULATION BENCHMARK ON THERMAL-HYDRAULIC BEHAVIOUR OF LIGHT METAL LAYER*. in *ICONE30*. 2023. Kyoto, Japan.
16. Villiermaux, C. *Mod lisation physique et num rique de la convection naturelle dans une couche de fluide de faible rapport d'aspect dans le cadre des  tudes d'accidents graves de r acteurs   eau sous pression*. 1999.
17. Fischer, P.F. *Scaling limits for PDE-based simulation*. in *22nd AIAA Computational Fluid Dynamics Conference*. 2015.
18. Grossmann, S. and D. Lohse, *Thermal convection for large Prandtl numbers*. Phys Rev Lett, 2001. **86**(15): p. 3316-9.
19. Shishkina, O., et al., *Boundary layer structure in turbulent thermal convection and its consequences for the required numerical resolution*. New journal of Physics, 2010. **12**(7): p. 075022.
20. Bian, B., D. Dovizio, and W. Villanueva, *Direct numerical simulation of an internally heated natural convection in a hemispherical geometry*. International Journal of Heat and Mass Transfer, 2023. **submitted**.
21. Deville, M.O., P.F. Fischer, and E.H. Mund, *High-Order Methods for Incompressible Fluid Flow*. Cambridge Monographs on Applied and Computational Mathematics. 2002, Cambridge: Cambridge University Press.
22. <https://doc.vega.izum.si/>.
23. Shams, A., *Towards the accurate numerical prediction of thermal hydraulic phenomena in corium pools*. Annals of Nuclear Energy, 2018. **117**: p. 234-246.